



**HAL**  
open science

## **Beam shaping to enhance zero group velocity Lamb mode generation in a composite plate and nondestructive testing application**

Frédéric Faëse, Samuel Raetz, Nikolay Chigarev, Charfeddine Mechri, James Blondeau, Benjamin Campagne, Vitali Goussev, Vincent Tournat

### ► **To cite this version:**

Frédéric Faëse, Samuel Raetz, Nikolay Chigarev, Charfeddine Mechri, James Blondeau, et al.. Beam shaping to enhance zero group velocity Lamb mode generation in a composite plate and nondestructive testing application. *NDT & E International*, 2017, 85, pp.13 - 19. 10.1016/j.ndteint.2016.09.003 . hal-01889431v1

**HAL Id: hal-01889431**

**<https://univ-lemans.hal.science/hal-01889431v1>**

Submitted on 6 Oct 2018 (v1), last revised 27 Apr 2019 (v2)

**HAL** is a multi-disciplinary open access archive for the deposit and dissemination of scientific research documents, whether they are published or not. The documents may come from teaching and research institutions in France or abroad, or from public or private research centers.

L'archive ouverte pluridisciplinaire **HAL**, est destinée au dépôt et à la diffusion de documents scientifiques de niveau recherche, publiés ou non, émanant des établissements d'enseignement et de recherche français ou étrangers, des laboratoires publics ou privés.

1     Beam shaping to enhance zero group velocity Lamb  
2             mode generation in a composite plate and  
3             nondestructive testing application

4     Frédéric Faëse<sup>a,b</sup>, Samuel Raetz<sup>b,\*</sup>, Nikolay Chigarev<sup>b</sup>, Charfeddine Mechri<sup>b</sup>,  
5         James Blondeau<sup>b</sup>, Benjamin Campagne<sup>c</sup>, Vitalyi E. Gusev<sup>b</sup>, Vincent  
6             Tournat<sup>b,1,\*\*</sup>

7             <sup>a</sup>*IRT Jules Verne, Chemin du Chaffault, 44340 BOUGUENNAIS - France*

8             <sup>b</sup>*Université du Maine, CNRS, LAUM UMR 6613, Av. O. Messiaen, 72085 LE MANS  
9             Cedex 9 - France*

10            <sup>c</sup>*Airbus Group Innovations, Chemin du Chaffault, 44340 BOUGUENNAIS - France*

---

11    **Abstract**

Zero group velocity (ZGV) Lamb modes have already shown their potential in nondestructive testing applications as they are sensitive to the sample structural characteristics. In this paper, we first consider an aluminum sample to validate a method based on the beam shaping of the generation laser. This method is proven to enhance ZGV Lamb modes in aluminum, and then advantageously applied to a composite material plate. Finally, based on the proposed method, scanning the sample over healthy and flawed zones demonstrates the ability to detect subsurface flaws.

12    *Keywords:* Laser ultrasonics, Composite materials, Zero Group Velocity  
13    Lamb modes, NDT

---

\*Corresponding author

\*\*Principal corresponding author

*Email addresses:* [samuel.raetz@univ-lemans.fr](mailto:samuel.raetz@univ-lemans.fr) (Samuel Raetz),  
[vincent.tournat@univ-lemans.fr](mailto:vincent.tournat@univ-lemans.fr) (Vincent Tournat)

<sup>1</sup>Currently at: John A. Paulson School of Engineering and Applied Science, Harvard University, Cambridge, MA 02138, USA

*Preprint submitted to NDT&E International*

*May 3, 2016*

## 14 **1. Introduction**

15 Laser ultrasonics is a more and more widespread nondestructive testing  
16 method as it shows specific advantages compared to conventional ultrasonic  
17 methods based on transducers or EMATs. Particularly, it has a high spatial  
18 resolution, a large bandwidth, and it is non-contact [1]. Thanks to these fea-  
19 tures, laser ultrasonic techniques allow characterizing the mechanical prop-  
20 erties and/or evaluating the structural health of materials, even where the  
21 tested samples present complex geometry and/or are subjected to extreme  
22 conditions such as high temperatures [2]. Up to now, applications of laser  
23 ultrasonic methods have already proved their potential in nondestructive  
24 testing of composite materials. They have been implemented successfully to  
25 detect delaminations with a propagative Lamb waves analysis [3] or by laser  
26 tapping [4]. They have also the ability to detect fiber breakage or matrix  
27 cracking via the scanning laser source technique [5] or even porosity thanks  
28 to an ultrasonic spectroscopy method [6].

29 Guided waves have been used in composite samples testing and evalua-  
30 tion because of their ability to detect a defect at a long propagation distance  
31 from the acoustic source position. Yet, the defect position is hard to pre-  
32 cisely estimate at a single interface at any position through the laminate [3].  
33 As well, a lateral position estimation needs methods with a transducer raster  
34 scan like the SAFT method [7] or transducer arrays like the topological imag-  
35 ing technique [8]. For ten years, some specific non-propagative Lamb modes  
36 called zero group velocity (ZGV) Lamb modes have been studied and already  
37 applied to defect detection. Considering a dispersion curve representing the  
38 angular frequency  $\omega$  as a function of the wave number  $k$ , these specific modes

39 are located in the points of a non-zero wave number  $k$  where the slope of this  
40 curve is horizontal, i.e.  $d\omega/dk = 0$ . Characterized by a high quality factor,  
41 these modes are used for instance to measure thickness variations due to  
42 corrosion, to detect disbonding or to determine elastic constants [9, 10]. A  
43 method based on the ZGV Lamb modes offers the advantages of being local  
44 and having a spatial resolution of the order of the plate thickness [10]. One  
45 objective of this article is to report on the effect of a flaw in a composite  
46 plate on ZGV Lamb modes.

47 The challenges to address when generating ZGV Lamb modes in com-  
48 posite plates are numerous. Firstly, the composite plates usually have a low  
49 damage threshold. For instance, the sample used in this paper showed fiber  
50 whitening at about  $5 \text{ MW.cm}^{-2}$  with a 1064 nm-wavelength laser, whereas  
51 the threshold for aluminum in the same experimental conditions is about 50  
52  $\text{MW.cm}^{-2}$  [11]. Secondly, as composite surfaces are matt and diffusive for  
53 light, ultrasonic waves are hardly detectable using non-contact optical tech-  
54 niques. Thirdly, quality factors of ZGV Lamb modes are strongly reduced  
55 because of the resin viscoelasticity leading to a strong sound attenuation in  
56 composite plates. Note that ZGV Lamb modes could even not exist, regard-  
57 ing the anisotropic mechanical properties of the material; nevertheless, this  
58 is out of the focus of this paper.

59 In this work, elastic waves are generated in an aluminum plate or a com-  
60 posite plate by a pulsed laser and detected using an interferometer. By  
61 varying the focusing of the pump laser beam, it is possible to favor the  
62 generation of either the propagating modes or the ZGV modes in the plate.  
63 Especially, considering a circular laser spot as the thermoelastic source, ZGV

64 Lamb modes are efficiently excited when the spot radius is about the plate  
65 thickness [12]. It is first shown that ZGV Lamb modes can be enhanced  
66 or reduced in an aluminum plate thanks to a specific beam shaping of the  
67 generation laser [13–15]. Then, the same method is advantageously applied  
68 to the healthy zone of a composite plate. Finally, a damaged region of the  
69 same composite plate is considered and the influences of the flaw on the  
70 ZGV Lamb modes are analyzed. Before going into details, the mechanical  
71 properties of the tested sample and the experimental setups are introduced.

## 72 **2. Mechanical properties of the tested sample and experimental** 73 **setups**

74 Since it is here proposed to study the influence of flaws on ZGV Lamb  
75 modes in a plate of composite material by using a beam-shaping mask to  
76 selectively generate a specific ZGV mode, it is important to know the me-  
77 chanical properties of the tested material in order to design the beam-shaping  
78 mask. We will show that the optimal geometrical properties of the beam-  
79 shaping mask for a particular ZGV mode generation depend on the ZGV  
80 wavelength in the sample. In the framework of industrial nondestructive  
81 testing (NDT), mechanical properties of the composite materials are already  
82 well characterized. Hence, the wavelengths of the ZGV modes that can be  
83 generated in the sample can be known. Here the mechanical properties of the  
84 composite sample were first characterized in order to determine an interesting  
85 ZGV mode and then to make the appropriate beam-shaping mask.

86 In order to predict the dispersion curve of the composite plate, both the  
87 density and the elastic constants have to be determined. First, the volu-  
88 metric mass density of the composite sample has been estimated thanks to

89 Archimedes principle to be  $\rho_{comp} \approx 1540 \text{ kg.m}^{-3}$ . Second, the elastic con-  
 90 stants have been determined thanks to a method explained in Refs. [16]  
 91 and [17]. Based on appropriate A-scans, plane wavefronts are synthesized  
 92 by summing the signals with suitable delays. By changing the synthesized  
 93 propagation angle, quasi-longitudinal and quasi-transversal time of flights are  
 94 semi-automatically recorded. Finally, the theoretical slowness curve that fits  
 95 the experimental one is determined, thanks to a minimization method. This  
 96 leads to the following estimation of the elastic constants:  $C_{11} = 13.4 \text{ GPa}$ ,  
 97  $C_{12} = 3.00 \text{ GPa}$ ,  $C_{22} = 21.36 \text{ GPa}$ , and  $C_{55} = 3.64 \text{ GPa}$ . Note that these  
 98 constants have been obtained by assuming that the composite plate is trans-  
 99 versely isotropic relative to an axis normal to the surface. Finally, from the  
 100 measured plate thickness,  $d_{comp} \approx 3.2 \text{ mm}$ , the wavelength of the first ZGV  
 101 Lamb mode in the composite plate can be estimated with a precision that is  
 102 sufficient for the method we propose:  $\lambda_{ZGV}^{comp} \approx 15.3 \text{ mm}$ .

103 Due to the low damage threshold of composite materials, the choice has  
 104 been done to experimentally use an extended line source instead of a circular  
 105 spot, in order to lower the source power density on the sample while keeping  
 106 sufficiently large displacement amplitude. Theoretically, using an infinitely  
 107 long and thin thermoelastic line source, the amplitude of the surface displace-  
 108 ment due to a ZGV Lamb mode as a function of the distance from the line  
 109 source is a pure cosine function, since it results from the interference of two  
 110 counter-propagative Lamb modes having the same wave number, i.e. of the  
 111 form  $e^{jk_{ZGV}x}$  and  $e^{-jk_{ZGV}x}$ . In the case of a finite line source, the amplitude  
 112 varies as an intermediate function between the pure cosine function and a  
 113 Bessel function [18], the latter standing for the theoretical spatial distribu-

114 tion of ZGV Lamb modes in the case of a point surface source [12]. In order  
 115 to selectively generate the first ZGV Lamb mode and to increase the total in-  
 116 cident laser power while keeping the power density constant, we propose here  
 117 to use multiple finite line sources using an appropriate beam-shaping mask.  
 118 As illustrated in Fig. 1, using the beam-shaping mask allows the generation  
 119 laser beam to be shaped with periodic slits whose spacing matches the ZGV  
 120 wavelength, thereby producing a constructive interference of the ZGV Lamb  
 121 modes generated by each line source.

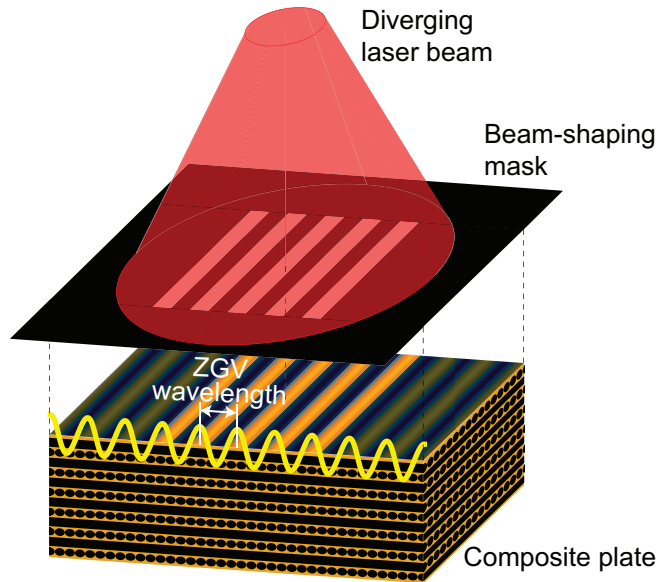


Figure 1: (color online) Illustration of the ZGV Lamb mode generation using a beam-shaping mask. The generation laser beam is shaped with periodic slits whose spacing matches the ZGV wavelength.

122 In order to analyze the ZGV Lamb mode generation using a shaped laser  
 123 beam, an experimental setup schematized in Fig. 2 has been implemented.  
 124 The generation laser is an Nd:YAG laser (Spitlight Compact 400, InnoLas

125 Laser GmbH, Germany) emitting 10 ns pulses at 1064 nm. The pulse energy  
126 is limited to a few tens of mJ in order to remain below the damage threshold  
127 and to avoid fiber whitening. This limitation of the laser energy is performed  
128 using two polarizing beam splitters (PBS) and a half-wave plate ( $\lambda/2$ ) as  
129 schematized in Fig. 2. Thanks to a negative lens, the whole beam shaping  
130 mask is illuminated by the generation laser. This mask consists of a series  
131 of transparent and opaque patterns (Fig. 1) printed on transparency films  
132 by a laser printer. Two identical masks are placed one after the other in  
133 the close vicinity of the plate in order to obtain a sufficient contrast. The  
134 normal surface displacement due to ultrasonic waves is detected on the other  
135 side of the sample by a two-wave mixing (TWM) interferometer (LU-TWM-  
136 ASGA, Tecnar Canada) whose bandwidth ranges from about 1 MHz to 40  
137 MHz [19]. Note that the bandpass spectrum of the interferometer filter is  
138 smooth and still allows to detect displacement with frequency component  
139 down to about 300 kHz. The TWM is using a CW Nd:YAG laser, the beam  
140 of which is guided through an optical fiber to the TWM head including a  
141 neutral density filter and the focusing/collecting lens. The TWM head is  
142 mounted on a motorized linear stage so that the detection point is scannable  
143 over the sample. A second motorized linear stage can also be used to scan  
144 the sample in front of fixed generation pattern and detection point. Since  
145 generation and detection of elastic waves are on opposite sides, this setup is  
146 referred to as the transmission setup in the following.

147 A second setup has been used in this study, with generation and detection  
148 on the same side, which is referred to as the reflection setup in the following.  
149 It is identical to the transmission setup, except that both generation laser



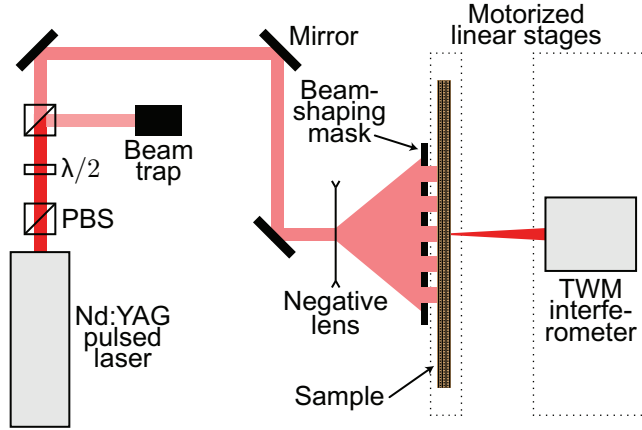


Figure 2: (color online) Schematics of the experimental transmission setup.

150 beam and TWM laser beam illuminate the same side of the sample, and  
 151 that the generation laser beam is frequency doubled in order not to dazzle  
 152 the TWM interferometer photodiode that is sensitive to 1064 nm radiation.  
 153 This setup can particularly be useful for a robot inspection and can give  
 154 additional information for a flaw characterization as it will be discussed in the  
 155 following: where the transmission setup detects a flaw without information  
 156 on its in-depth position, we will see that the reflection setup is able to give  
 157 information on the flaw position with respect to the depth.

158 Before applying the proposed method to the detection of a flaw in a  
 159 composite plate, it is first proposed to focus on the interest of using a beam-  
 160 shaping mask to enhance the ZGV Lamb modes in two samples: first, an  
 161 aluminum plate for trivial evidence, and then a composite plate.

162 **3. ZGV Lamb modes enhancement in aluminum and composite**  
163 **plates**

164 In order to validate preliminary results obtained with the transmission  
165 setup schematized in Fig. 2, Fig. 3 presents the experimental results obtained  
166 in an 4.1 mm-thick aluminum plate using a single thermoelastic line source  
167 of dimensions 4.1 x 20 mm<sup>2</sup>. Figs. 3(a)-(b) are slightly saturated in order to  
168 improve readability.

169 The time domain B-scan [Fig. 3(a)] represents the normal surface dis-  
170 placement amplitude as a function of time and the TWM head position.  
171 The signals have been registered over 200  $\mu$ s with the TWM head position  
172 ranging from  $-50$  mm to  $+50$  mm with a 0.5 mm step. Two different kinds  
173 of modes are visible: (i) the propagating modes starting at the origin in time  
174 and space, and (ii) the ZGV Lamb modes that are visible in time after the  
175 propagating modes. The ZGV modes are evidenced by a succession of max-  
176 ima and minima in time and space, typical of the single frequency and the  
177 interferential nature of the ZGV modes.

178 The frequency domain B-scan [Fig. 3(b)] represents the spectral ampli-  
179 tude module of each A-scan constituting the time domain B-scan as a func-  
180 tion of the TWM head position. Each spectrum constituting the frequency  
181 domain B-scan has been calculated over the whole corresponding A-scan. At  
182 the first, i.e. lowest, expected ZGV Lamb mode frequency,  $f_{ZGV}^{Al} \approx 694$  kHz,  
183 there is a maxima and minima succession in space that is typical of ZGV  
184 Lamb modes obtained with a thermoelastic line source. When zooming at  
185 the ZGV frequency [Fig. 3(c)], the first ZGV peak amplitude as a func-  
186 tion of the TWM head position (solid) shows the expected theoretical shape

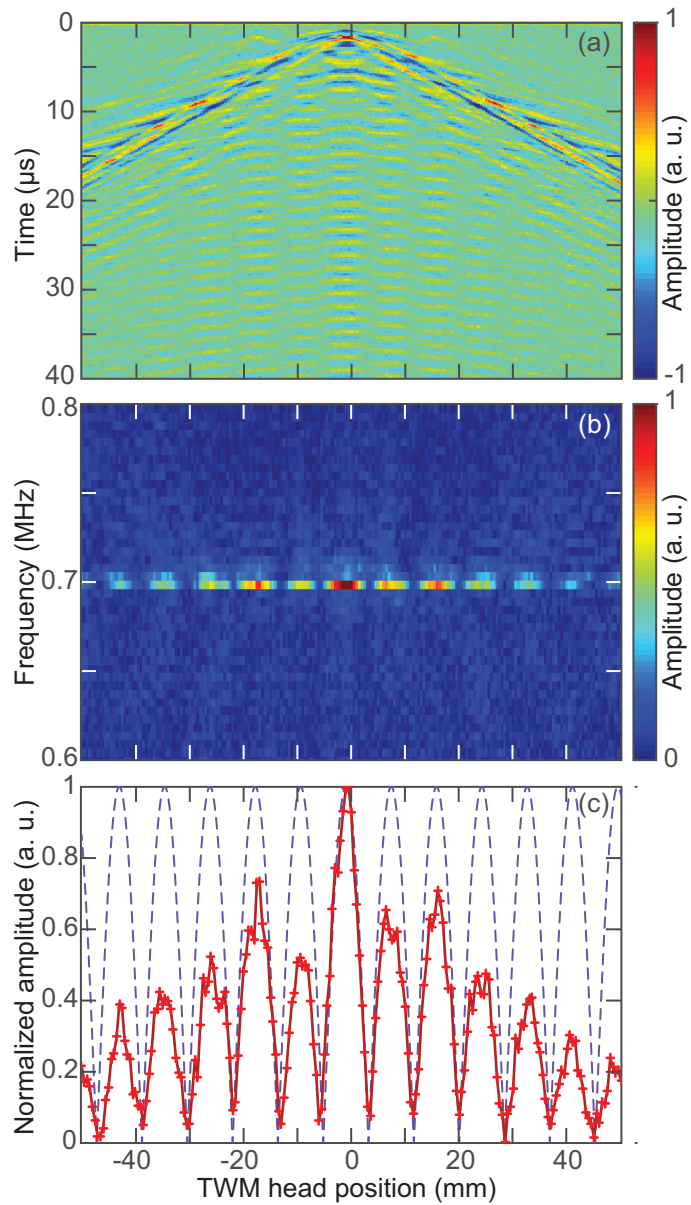


Figure 3: (color online) The thermoelastic source is a line  $4.1 \times 20 \text{ mm}^2$ : (a) time domain and (b) frequency domain B-scans as a function of the TWM head position. (c) First ZGV peak amplitude vs. TWM head position: experimental (solid) and theoretical (dashed) curves.

187 (dashed), especially regarding the minima. As expected theoretically, the  
 188 amplitude of the experimental curve decays with the distance from the line  
 189 source position because of the line source finite dimensions.

190 It is now proposed to compare this result obtained with a single line  
 191 source to the results obtained with a shaped source composed of lines spaced  
 192 by either  $\lambda_{ZGV}^{Al}$  or  $\lambda_{ZGV}^{Al}/2$ . Figure 4 presents the amplitude of the first ZGV  
 193 peak as a function of the TWM head position when the thermoelastic source  
 194 is made of: a single line (solid), multiple lines spaced by  $\lambda_{ZGV}^{Al}$  (dashed),  
 195 and multiple lines spaced by  $\lambda_{ZGV}^{Al}/2$  (dash-dotted). The Frobenius norm  
 196 (Euclidian norm) of each normal displacement field is used to normalize each  
 197 corresponding curve in Fig. 4, in order for the changes in the absorbed laser  
 198 power between the different cases to be compensated.

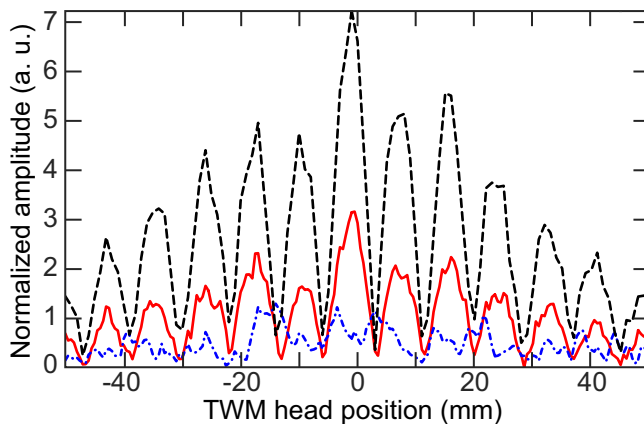


Figure 4: (color online) Normalized first ZGV peak amplitude vs. TWM head position when the thermoelastic source is a single line (solid), multiple lines spaced by  $\lambda_{ZGV}^{Al}$  (dashed) and multiple lines spaced by  $\lambda_{ZGV}^{Al}/2$  (dash-dotted).

199 When the lines are spaced by  $\lambda_{ZGV}^{Al}$ , the ZGV Lamb modes are enhanced:  
 200 they interfere constructively. On the contrary, when the lines are spaced

201 by  $\lambda_{ZGV}^{Al}/2$ , the ZGV Lamb mode amplitudes are reduced: they interfere  
 202 destructively. As expected, a mask consisting of slits spaced by the ZGV  
 203 wavelength enhances the ZGV Lamb modes generation in aluminum com-  
 204 pared to a mask consisting of a single slit. The interest of this beam-shaping  
 205 method being demonstrated in a metal plate, it is now examined in the more  
 206 challenging case of a composite plate.

207 The beam-shaping mask used with the composite plate consists of three  
 208 slits spaced by  $\lambda_{ZGV}^{comp}$ . Figures 5(a)-(c) show the experimental results. Fig-  
 209 ure 5(a) stands for the time domain B-scan, while Fig. 5(b) shows the fre-  
 210 quency domain B-scan. Figures 5(a)-(b) are slightly saturated in order to  
 211 improve readability. The amplitude of the first ZGV peak with respect to the  
 212 TWM head position obtained for the three-line source (thick line) is com-  
 213 pared to the same amplitude obtained with a single line source (thin line) in  
 214 Fig. 5(c). The ZGV peak amplitudes in Fig. 5(c) are normalized following  
 215 the same method as the one described for aluminum.

216 The time domain B-scan [Fig. 5(a)] highlights the propagating modes  
 217 and we slightly see the ZGV Lamb modes. The frequency domain B-scan  
 218 [Fig. 5(b)] points out the ZGV Lamb modes at the frequency  $f_{ZGV}^{comp} \approx 0.480$  MHz,  
 219 which is confirmed by Fig. 5(c). Indeed, as ZGV peaks correspond to energy  
 220 peaks, they are expected to be spaced by half the ZGV wavelength, that  
 221 is to say that ZGV peaks are expected to be located in the middle of each  
 222 illuminated slits as well as centrally located between two adjacent slits. As  
 223 Fig. 5(c) shows these peaks on the slits location (under black arrows) and  
 224 centrally located between two adjacent slits (under gray arrows), this result  
 225 tends to prove the enhancement of the ZGV mode in the composite plate

226 thanks to the proposed beam-shaping mask.

227 In order to obtain Fig. 5(c), the ZGV peak amplitude was measured as the  
228 maximum spectral amplitude module between 0.475 MHz and 0.485 MHz.  
229 This frequency range can be related to a possible sample thickness variation  
230 since the product of the ZGV mode frequency  $f_{ZGV}$  by the sample thickness is  
231 constant. Hence, the average ZGV frequency  $(f_{ZGV})_0$  and the ZGV frequency  
232 variation  $\Delta f_{ZGV}$  on the one hand, and the average sample thickness  $d_0$  and  
233 the sample thickness variation  $\Delta d$  on the other hand, are related to each  
234 other:

$$235 \quad \frac{\Delta d}{d_0} = -\frac{\Delta f_{ZGV}}{(f_{ZGV})_0}. \quad (1)$$

236 The range [0.475-0.485] MHz leads to a thickness variation  $\Delta d$  of about  
237  $\pm 33 \mu\text{m}$ . This sample thickness variation is very small and it is consistent  
238 with the precision of the sample fabrication process.

239 As the beam-shaping method is validated to enhance ZGV Lamb modes  
240 in the composite plate, a suitable mask with slits spaced by  $\lambda_{ZGV}$  is now  
241 used for an NDT application.

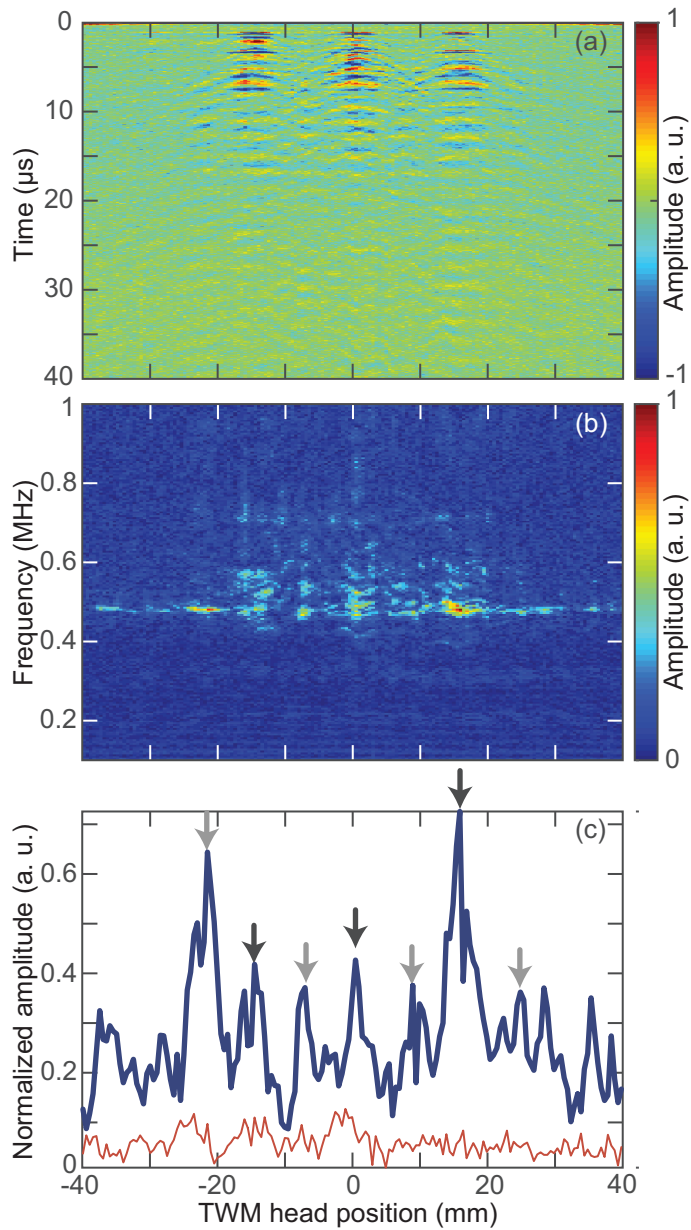


Figure 5: (color online) Results obtained in the composite plate with a thermoelastic source made of three lines: (a) time domain and (b) frequency domain B-scans vs. TWM head position. (c) Normalized amplitude of the first ZGV peak vs. TWM head position (thick line) compared with the result obtained with a single line source (thin line).

242 **4. NDT application in a composite plate**

243 The reflection setup described in Sec. 2 is now used to scan the composite  
244 plate in front of both spatially fixed Nd:YAG frequency doubled laser beam  
245 and TWM interferometer beam, the latter being focused to a point in the  
246 middle of the beam shaping mask (middle line). As quickly explained in  
247 Sec. 2, the choice of using a reflection setup instead of the so-far used trans-  
248 mission setup is twofold: (i) this is closer to industrial applicability, and (ii)  
249 the flaw in the tested sample is such that, at the flaw location, there is no  
250 direct transmission of the elastic waves through the flaw, making the lateral  
251 detection of the flaw easy but not the in-depth location. We will see that  
252 using a reflection setup can lead to this in-depth characterization of the flaw.

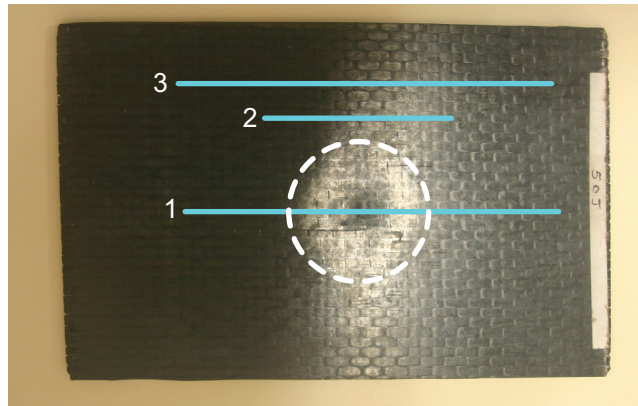


Figure 6: (color online) Composite sample and representation of the scan lines (solid). Dashed white line circle: maximum size of the flaw observed optically.

253 The composite sample presented in Fig. 6 has been impacted by a 50 J  
254 centered shock. The 50 J shock was obtained thanks to the drop of a hemi-  
255 spherical mass with a diameter of 25 mm. The sample was clamped on a  
256 bearing having a 40 mm-diameter hole, centered with respect to the drop



257 mass axis. The first scan line (line 1) crosses the impact whereas the second  
 258 scan line (line 2) is near the impact location and the third scan line (line 3) is  
 259 far from the impact location. Regarding line 3, note that the thermoelastic  
 260 line sources are at least 5 mm away from both the plate edge and the impact  
 261 location, whatever the plate position during the scan.

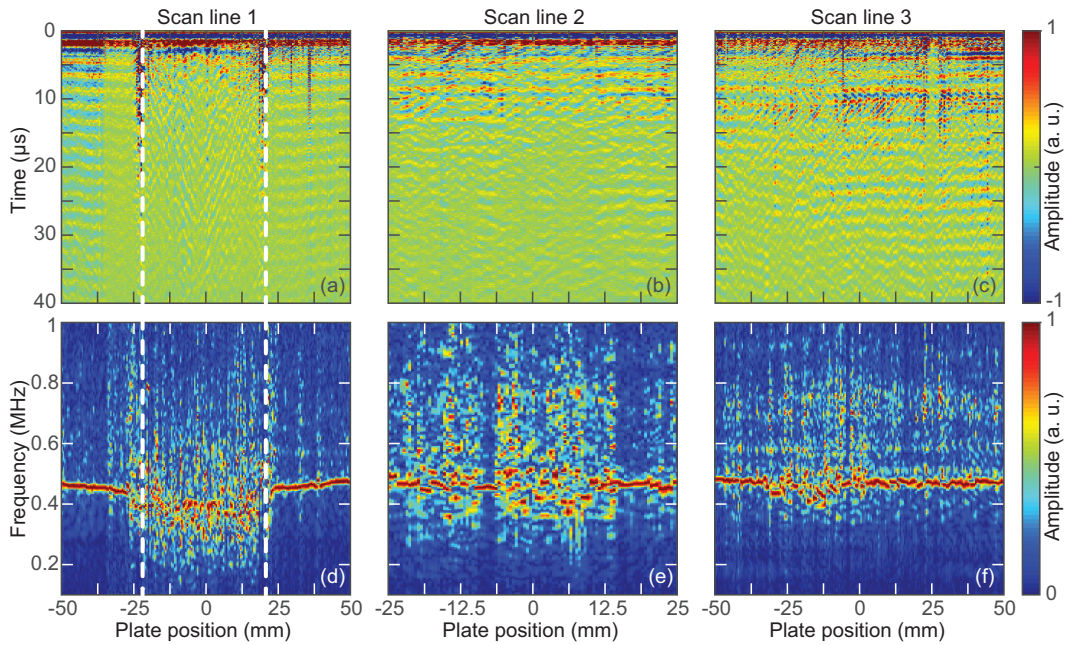


Figure 7: (color online) Time domain B-scans of the composite plate when the scan line is: line 1 across the impact location (a), line 2 near the impact location (b), and line 3 far from the impact location (c). The related frequency domain B-scans obtained with a Hann time window (respectively d, e and f). Dashed white lines: maximum dimension of the flaw observed optically.

262 The time domain B-scan signals have been registered over  $200 \mu\text{s}$  with  
 263 the plate position ranging from  $-50 \text{ mm}$  to  $+50 \text{ mm}$  [Fig. 7(a) and Fig. 7(c)]  
 264 or from  $-25 \text{ mm}$  to  $+25 \text{ mm}$  [Fig. 7(b)] with a  $0.5 \text{ mm}$  step. Each A-scan for  
 265 a given plate position is numerically post-processed in order to have a zero

266 mean value over the useful signal duration, i.e. from 10  $\mu\text{s}$  to 100  $\mu\text{s}$ . The  
267 frequency domain B-scans have then been calculated over the whole time  
268 domain signals filtered by a Hann time window ranging from 0  $\mu\text{s}$  to 100  $\mu\text{s}$   
269 in order to emphasize the ZGV Lamb modes. The spectrum amplitude for a  
270 given plate position is normalized to its maximum.

271 In Fig. 7(a), the time domain B-scan across the impact location high-  
272 lights the impact edges marked by the dashed white lines (cf. also Fig. 6).  
273 Moreover, regular successions of maxima and minima in time, representative  
274 of ZGV oscillations, can be observed outside of the impact location (in a  
275 healthy zone) whereas the signal appears disturbed inside the impact loca-  
276 tion. The time domain B-scans near the impact location and far from the  
277 impact location [Fig. 7(b) and Fig. 7(c), respectively] show minor changes  
278 with the plate position and no flaw is clearly evidenced.

279 The frequency domain B-scan across the impact location [Fig. 7(d)] also  
280 clearly highlights the impact as only the ZGV frequency is visible outside  
281 the impact location whereas on the impact location the dominant frequency  
282 components are spread out over the range  $\sim 200 - 800$  kHz and show quick  
283 variations in space. Let us also notice that the ZGV frequency decreases  
284 almost linearly when the signal measurement gets closer to the impact. As  
285 the product  $f_{ZGV}$  by the thickness is constant, this shows that either the  
286 plate thickness increases with the impact vicinity (the 50 J impact has lead  
287 to a bulge at the vicinity of the impact) or the elastic moduli diminish.  
288 The frequency domain B-scan near the impact location [Fig. 7(e)] also shows  
289 changing multiple frequency components between  $-5$  mm and  $+15$  mm that  
290 could be due to the impact vicinity. Moreover, farther from the impact

291 location, i.e. between  $-25$  mm and  $-10$  mm, multiple frequency components  
292 also appear whereas this zone should be healthy. The frequency domain B-  
293 scan far from the impact location [Fig. 7(f)] shows that the main frequency  
294 component is the ZGV frequency below  $-30$  mm and above  $0$  mm; these zones  
295 can thus be considered as quasi-healthy zones. On the contrary, between  
296  $-30$  mm and  $0$  mm, a hidden flaw is detected. This confirms the previous  
297 result [Fig. 7(e)] highlighting a flaw on a zone that should be healthy.

298 These results have been compared to the composite plate inspection ob-  
299 tained with a system called LUCIE, the technical specifications of which are  
300 gathered in Ref. [20]. Note that the minimum laser fluence delivered by the  
301 pump laser ( $\text{CO}_2$ ,  $270$  mJ,  $100$  ns) in the LUCIE system is  $1.5 \text{ MW}\cdot\text{cm}^{-2}$ ,  
302 which is below the damage threshold of the composite. Figure 8 represents  
303 the C-scan inspection of the composite plate consisting in measuring the ratio  
304 of the second ultrasonic echo amplitude to the first ultrasonic echo ampli-  
305 tude as a function of the position on the plate. Note that the ratio can be  
306 done after filtering the collected raw data with a selective band-pass filter.  
307 LUCIE's data post-processing may also give an image (not shown in this pa-  
308 per) of the time of flight difference between the first and the second detected  
309 acoustic echo, although this image is not precise for in-depth localization of  
310 defects close to the surface. The presented scan (Fig. 8) shows two major  
311 results. First, the  $50$  J impact is very well identified by the centered zone  
312 that shows the lowest value. Second, on the healthy zone scanned previously  
313 (cf. line 3 in Fig. 6), the ratio has either values in  $[1.95\text{-}3.15]$  % that should  
314 be indicative of a real healthy zone or weak values lower than  $1.7$  % that  
315 are indicative of a flaw. This last result confirms the presence of the hidden

316 flaw detected previously along the scan line 3 by the method proposed by  
317 the authors.

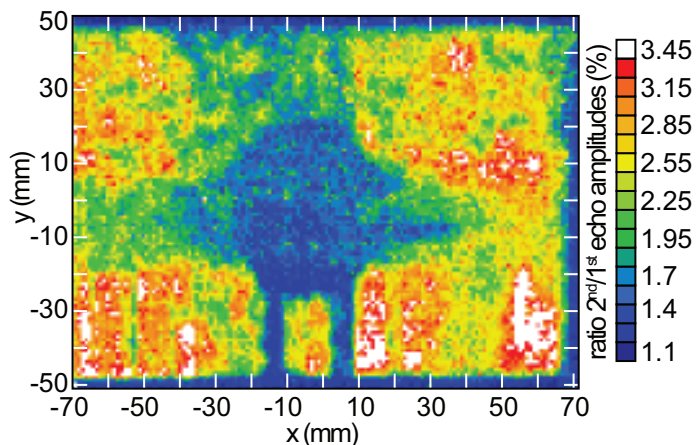


Figure 8: (color online) C-scan inspection of the composite plate obtained with the LUCIE system: ratio of the second ultrasonic echo amplitude to the first ultrasonic echo amplitude

318 Using the experimental transmission setup, a supplementary scan has  
319 been done along the scan line 1, the results of which is not presented in  
320 this paper. The observation is that, at the flaw location, no elastic wave is  
321 directly transmitted. This observation probably means that the 50 J impact  
322 produced a delamination inside the composite plate.

323 Let us consider that the impact produced a delamination inside the com-  
324 posite plate, hence splitting the plate into a minimum of two thinner plates  
325 one above the other. If we assume that laser generated ultrasonic waves  
326 interact only with the top plate, several mechanisms can explain why the  
327 frequency domain B-scans show multiple frequency components on the de-  
328 lamination location. A given frequency component different from the ZGV  
329 mode frequency of the plate can be due to a membrane resonance effect [21]

330 or to a local defect resonance [22]. It could even be due to another ZGV mode  
 331 frequency associated to a smaller thickness than the one of the plate. A flaw  
 332 resonance frequency  $f_r$  can be estimated by assuming a circular clamped  
 333 membrane:

$$334 \quad f_r = \frac{1.88h}{d^2} \sqrt{\frac{E}{\rho(1-\nu^2)}}, \quad (2)$$

335 where  $h$  and  $d$  are the flaw depth and diameter respectively, and  $E$ ,  $\rho$  and  $\nu$   
 336 are the sample Young's modulus, density and Poisson ratio respectively.

337 If we assume the following typical values:  $h = 100 \mu\text{m}$  (a ply thickness),  
 338  $d = 1.3 \text{ mm}$ ,  $E = 20 \text{ GPa}$ ,  $\rho = 1540 \text{ kg/m}^3$  and  $\nu = 0.2$ , this leads to a  
 339 typical value of flaw resonance frequency  $f_r \simeq 0.41 \text{ MHz}$ , which is in good  
 340 agreement with the frequency values observed in the frequency domain B-  
 341 scans in Fig. 7. This estimate suggests that a better knowledge of either  
 342 the flaw geometry or the local mechanical material properties is necessary to  
 343 develop a realistic model in relation to our experimental results. This could  
 344 lead in the future to quantitative estimates of defect parameters relevant for  
 345 the structural health assessment of composite structures.

## 346 5. Conclusion

347 We have presented a method enabling ZGV Lamb modes enhancement  
 348 thanks to the beam shaping of the generation laser, making use of a mask  
 349 with slits spaced by the ZGV wavelength. First, ZGV Lamb modes have  
 350 been analyzed in an aluminum plate to validate the possibility to enhance  
 351 or reduce their amplitude depending on the thermoelastic line sources spac-  
 352 ing. It has been shown that ZGV Lamb modes interfere constructively when  
 353 the line sources spacing equals the ZGV wavelength whereas they interfere

354 destructively when the spacing is halved.

355 After the thorough characterization of a composite plate that resulted  
356 in the ZGV wavelength determination, the beam-shaping method has been  
357 applied to the composite sample. Experimental results demonstrate a ZGV  
358 Lamb mode enhancement, hence validating the beam-shaping method also  
359 in the case of a composite sample. Finally, by scanning over the sample,  
360 the measured signal frequency content near the ZGV frequency has proven  
361 its ability to distinguish between healthy zones and an impacted zone of a  
362 composite plate, and also to detect flaw zones that are not visually detectable.  
363 The next step could possibly be to extract quantitative information from the  
364 dominant frequencies of the B-scans compared to those predicted by the  
365 mechanical models of the defects.

## 366 **6. Acknowledgments**

367 This presentation is part of the LUCITA project managed by IRT Jules  
368 Verne (French Institute in Research and Technology in Advanced Manu-  
369 facturing Technologies for Composite, Metallic and Hybrid Structures). The  
370 authors wish to associate the industrial and academic partners of this project:  
371 Airbus Group Innovations and STELIA Aerospace; EMN-Subatech and LAUM  
372 respectively.

## 373 **References**

- 374 [1] J. Cooper, R. A. Crosbie, R. J. Dewhurst, A. D. W. McKie, and S. B.  
375 Palmer, Surface acoustic wave interactions with cracks and slots: A  
376 noncontacting study using lasers, *IEEE Trans. Ultrason. Ferroelectr.*  
377 *Freq. Control.* **33**, 462–470 (1986).

- 378 [2] D. W. Schindel, D. A. Hutchins, S. T. Smith, and B. Farahbakhsh,  
379 Hightemperature pulsed photoacoustic studies of surface waves on solids,  
380 *J. Acoust. Soc. Am.* **95**, 2517–2524 (1994).
- 381 [3] N. Guo and P. Cawley, The interaction of Lamb waves with delamina-  
382 tions in composite laminates, *J. Acoust. Soc. Am.* **94**, 2240–2246 (1993).
- 383 [4] A. Blouin, C. Néron, B. Campagne, and J.-P. Monchalain, Applications  
384 of laser-ultrasonics and laser-tapping to aerospace composite structures.,  
385 in *Conference proceedings of 17th WCNDT. Shanghai.*, page 7 (2008).
- 386 [5] P. A. Fomitchov, A. K. Kromin, S. Krishnaswamy, and J. D. Achenbach,  
387 Imaging of damage in sandwich composite structures using a scanning  
388 laser source technique, *Compos. Part B-Eng.* **35**, 557–562 (2004), marine  
389 Composites.
- 390 [6] A. A. Karabutov and N. B. Podymova, Quantitative analysis of the  
391 influence of voids and delaminations on acoustic attenuation in CFRP  
392 composites by the laser-ultrasonic spectroscopy method, *Compos. Part*  
393 *B-Eng.* **56**, 238–244 (2014).
- 394 [7] M. Spies and W. Jager, Synthetic aperture focusing for defect recon-  
395 struction in anisotropic media, *Ultrasonics* **41**, 125–131 (2003).
- 396 [8] S. Rodriguez, M. Castaings, M. Deschamps, and E. Ducasse, Topological  
397 imaging of defects in anisotropic plates, in V. Le Cam, L. Mevel, and  
398 F. Schoefs, editors, *EWSHM - 7th European Workshop on Structural*  
399 *Health Monitoring*, pages 1155–1162 (2014).

- 400 [9] D. Clorennec, C. Prada, and D. Royer, Local and noncontact measure-  
401 ments of bulk acoustic wave velocities in thin isotropic plates and shells  
402 using zero group velocity Lamb modes, *J. Appl. Phys.* **101**, 034908  
403 (2007).
- 404 [10] D. Clorennec, C. Prada, and D. Royer, Laser ultrasonic inspection of  
405 plates using zero-group velocity Lamb modes, *IEEE Trans. Ultrason.*  
406 *Ferroelectr. Freq. Control.* **57**, 1125–1132 (2010).
- 407 [11] J. F. Ready, in J. F. Ready, editor, *Effects of High-Power Laser Radia-*  
408 *tion*, chapter 3, pages 67–125, Academic Press (1971).
- 409 [12] O. Balogun, T. W. Murray, and C. Prada, Simulation and measure-  
410 ment of the optical excitation of the  $S_1$  zero group velocity Lamb wave  
411 resonance in plates, *J. Appl. Phys.* **102**, 064914 (2007).
- 412 [13] A. Bennis, A. M. Lomonosov, Z. H. Shen, and P. Hess, Laser-based mea-  
413 surement of elastic and mechanical properties of layered polycrystalline  
414 silicon structures with projection masks, *Appl. Phys. Lett.* **88**, 101915  
415 (2006).
- 416 [14] A. A. Maznev and A. G. Every, Surface acoustic waves with negative  
417 group velocity in a thin film structure on silicon, *Appl. Phys. Lett.* **95**,  
418 011903 (2009).
- 419 [15] C. Grünsteidl, I. A. Veres, J. Roither, P. Burgholzer, T. W. Murray, and  
420 T. Berer, Spatial and temporal frequency domain laser-ultrasound ap-  
421 plied in the direct measurement of dispersion relations of surface acoustic  
422 waves, *Appl. Phys. Lett.* **102**, 011103 (2013).



- 423 [16] F. Reverdy and B. Audoin, Elastic constants determination of  
424 anisotropic materials from phase velocities of acoustic waves generated  
425 and detected by lasers, *J. Acoust. Soc. Am.* **109**, 1965–1972 (2001).
- 426 [17] B. Hosten and B. Castagnede, Optimisation du calcul des constantes  
427 élastiques à partir des mesures de vitesses d’une onde ultrasonore, *C. R.  
428 Acad. Sc. Paris*, **296**, 297–300 (1983).
- 429 [18] S. Raetz, J. Laurent, T. Dehoux, D. Royer, B. Audoin, and C. Prada,  
430 Effect of refracted light distribution on the photoelastic generation of  
431 zero-group velocity Lamb modes in optically low-absorbing plates, *J.  
432 Acoust. Soc. Am.* **138**, 3522–3530 (2015).
- 433 [19] R. K. Ing and J. Monchalain, Broadband optical detection of ultrasound  
434 by two-wave mixing in a photorefractive crystal, *Appl. Phys. Lett.* **59**,  
435 3233–3235 (1991).
- 436 [20] B. Campagne, H. Voillaume, L. Gouzerh, and F. Bentouhami, Laser ul-  
437 trasonic developments for NDT of aeronautic composite parts, in *13th  
438 International Symposium on Nondestructive Characterization of Mate-  
439 rials (NDCM-XIII) 2013, Le Mans, France*, volume 19, NDT.net, The  
440 e-Journal of Nondestructive Testing & Ultrasonics (2014).
- 441 [21] P. Cawley and C. Theodorakopoulos, The membrane resonance method  
442 of non-destructive testing, *J. Sound Vibrat.* **130**, 299–311 (1989).
- 443 [22] I. Solodov, J. Bai, S. Bekgulyan, and G. Busse, A local defect resonance  
444 to enhance acoustic wave-defect interaction in ultrasonic nondestructive  
445 evaluation, *Appl. Phys. Lett.* **99**, 211911 (2011).

446 **List of Figures**

447 1 (color online) Illustration of the ZGV Lamb mode generation  
448 using a beam-shaping mask. The generation laser beam is  
449 shaped with periodic slits whose spacing matches the ZGV  
450 wavelength. . . . . 6

451 2 (color online) Schematics of the experimental transmission setup. 8

452 3 (color online) The thermoelastic source is a line 4.1 x 20 mm<sup>2</sup>:  
453 (a) time domain and (b) frequency domain B-scans as a func-  
454 tion of the TWM head position. (c) First ZGV peak amplitude  
455 vs. TWM head position: experimental (solid) and theoretical  
456 (dashed) curves. . . . . 10

457 4 (color online) Normalized first ZGV peak amplitude vs. TWM  
458 head position when the thermoelastic source is a single line  
459 (solid), multiple lines spaced by  $\lambda_{ZGV}^{Al}$  (dashed) and multiple  
460 lines spaced by  $\lambda_{ZGV}^{Al}/2$  (dash-dotted). . . . . 11

461 5 (color online) Results obtained in the composite plate with a  
462 thermoelastic source made of three lines: (a) time domain and  
463 (b) frequency domain B-scans vs. TWM head position. (c)  
464 Normalized amplitude of the first ZGV peak vs. TWM head  
465 position (thick line) compared with the result obtained with  
466 a single line source (thin line). . . . . 14

467 6 (color online) Composite sample and representation of the scan  
468 lines (solid). Dashed white line circle: maximum size of the  
469 flaw observed optically. . . . . 15

470	7	(color online) Time domain B-scans of the composite plate	
471		when the scan line is: line 1 across the impact location (a),	
472		line 2 near the impact location (b), and line 3 far from the	
473		impact location (c). The related frequency domain B-scans	
474		obtained with a Hann time window (respectively d, e and f).	
475		Dashed white lines: maximum dimension of the flaw observed	
476		optically. . . . .	16
477	8	(color online) C-scan inspection of the composite plate ob-	
478		tained with the LUCIE system: ratio of the second ultrasonic	
479		echo amplitude to the first ultrasonic echo amplitude . . . . .	19